Sink strength and dislocation bias of three-dimensional microstructures

Aaron A. Kohnert and Laurent Capolungo

Los Alamos National Laboratory, Los Alamos, New Mexico 87545, USA

Irradiation induces significant changes in the microstructure of structural materials, many of which are driven by the preferential capture of point defects at particular sinks, such as dislocations. To quantify the kinetics of defect absorption at sinks, theoretical models of radiation damage generally rely on the concept of sink strength. However, analytical approaches to estimating the sink strength of dislocations rely, in turn, on a series of geometrical assumptions, idealizing the dislocation network as a series of infinite straight dislocations or isolated loops, often with artificial boundary conditions. In this paper, we use a recently developed technique to quantify point defect capture in three-dimensional dislocation networks. We integrate this technique with discrete dislocation dynamics to analyze the sink strengths of realistic dislocation microstructures consisting of a mixture of edge, screw, and junction segments, complete with an accurate description of the strain fields these microstructures produce and the resultant energetic interactions experienced by point defects. We show that the effective kinetics for absorbing point defects can vary significantly with the arrangement of the microstructure with a strong dependence on the structure and character of its dislocation content and introduce a surrogate model for sink strength which incorporates these effects.

I. INTRODUCTION

In radiation environments, atomic scale collisions with energetic particles populate the lattice of crystalline materials with point defects and point defect clusters. The fate of such defects is determined by their ability to migrate and interact with either other defects and/or sinks, such as dislocations and grain boundaries. The kinetics and kinematics of point defect migration are determined both by gradients in the defect concentration as per Ficks law and by interaction with any elastic strain fields in the medium. These strain-mediated changes in transport kinetics are different for self-interstitial- and vacancy-type defects. Over time, the persistent arrival of an excess of one defect type or the other at a given sink results in the local accumulation or loss of mass such that defect by defect, atom by atom, the material's original structure transforms into a damaged structure. Consequently, long-term changes in the physical and mechanical properties of metals are often activated in full or in part by such strain interactions. Examples include void swelling which produces macroscopic changes in volume [1–5], radiation-induced climb which facilitates accelerated creep [6–9], and the formation of prismatic dislocation loops which promotes hardening [10–12]. The ability to predict nucleation and growth rates for these damage features depends on quantifying the strain state of a material in the undamaged and damaged microsturctures, respectively, and its effect on the current of various point defects and point defect clusters into the sinks present.

Quantitative theoretical descriptions of these processes are provided by mean-field rate theory (MFRT). In this approach, the individual, discrete sinks in a material are replaced by a homogeneous lossy medium, and the kinetics of defect absorption are quantified through the medium's sink strength. The defect concentrations, which in reality are complex func-tions of space, time, and the internal strain state, are similarly replaced by their averages. Ideally, the net rate of defect capture at each sink type in this homogenized system is identical to that of the real microstructure it is designed to replicate. However, it is not immediately evident how this homogenization procedure is best approached, and several competing methods have emerged [13–18]. The usual approach is to consider isolated sinks which do not interact and solve a simplified version of the point defect transport in an idealized geometry to deduce the defect flux to a given sink.

Macroscopic descriptions of microstructural evolution based on MFRT frequently neglect several crucial aspects of the physics of radiation damage. These include, but are not limited to, the clustering of point defects in cascades, the anisotropic properties of defects, the collective effects of dislocation structures, the resulting strain fields, and the mixed character of realistic dislocation structures. Molecular dynamics simulations have produced extensive knowledge of cascade structure and defect clustering [19–23], and these insights have been used to inform microstructure models over longer timescales [24–26]. Defect anisotropy has received significant attention as well [27,28], but the effects of the spatial correlation of dislocations and the collective effect of their strain fields are largely neglected in the generation of dislocation sink strengths to date. These latter concerns are the focus of the present paper as it is far from clear that a single infinite perfectly straight edge dislocation at the center of a cylindrical defect supply is an adequate surrogate for a three-dimensional (3D) dislocation network. The multiplicity of slip systems, the edge/screw character, the presence of junctions, and line curvature all leave lingering questions about whether the conventional sink strength calculations are representative of the net point defect currents into dislocations in real microstructures. These concerns are difficult to address

with analytical approaches. However, recently developed numerical techniques allow the point defect transport and absorption problem to be solved efficiently and accurately for complex arrangements of dislocations in statistically representative volumes, including a proper description of the internal strain field and its effects [29].

In this paper, we apply discrete dislocation dynamics (DDD) and spatially resolved rate theory to to quantify the net absorption rate of point defects at dislocations. This allows a critical assessment of the representativeness of particular sink strength estimates for dislocation networks and the ability of MFRT to represent three-dimensional dislocation networks as lossy media in general. Section II outlines the methodology for incorporating strain field interactions in the defect flux and calculating the resultant sink strengths for arbitrary three-dimensional dislocation networks. Section III quantifies the effect of dislocation arrangement on sink strength, first without, and then with the effect of strain field interactions. The analysis spans a series of increasingly realistic dislocation structures, beginning with purely periodic two-dimensional (2D) arrays, moving to randomized 3D arrangements of straight dislocations, and finally examining networks consisting of a complex tangle of dislocations of varying character and junction content. The organization of the microstructure and the character of the network promote significant changes in sink strength, particularly, with respect to the effect of internal strain. We develop a surrogate expression for the dislocation sinks strength which captures these effects, and its implications are discussed in Sec. IV.

II. METHODS

The sink strength and bias of dislocations is governed by the diffusive and strain-induced transport of point defects throughout the material, and ultimately the rate at which point defects reach dislocations as a consequence of these fluxes. One can write the conservation of the mass condition on the concentration c of a point defect population with source rate g as

$$\frac{dc}{dt} = -\boldsymbol{\nabla} \cdot \mathbf{J} + g, \tag{1}$$

where the flux J of a particular defect species can be decomposed into diffusive and drift components according to

$$J_i = -D_{ij}(c_{,j} + \beta c E_{,j}), \tag{2}$$

where subscripts preceded by commas refer to a partial derivative, D_{ij} is the (bulk) diffusion tensor for the defect, and β related to temperature as $1/k_b T$. Here, the interaction energy E is determined by the elastic strain state at the position the defect is located $\epsilon(\mathbf{r})$ and the point defect dipole tensor p in the ground-state configuration according to [30,31]

$$E(\mathbf{r}) = -p_{ij}\epsilon_{ij}(\mathbf{r}), \tag{3}$$

with a summation implied over repeated indices. Atomistic methods can also be used to find interaction energies [32–34], but in the exception of the core region, linear elasticity theory describes the strain state well, and the dipole representation supplies accurate energetics even for complex defects, such as small loops [35].

In principle, the diffusivity D may be anisotropic and will become a function of the strain state if the dipole tensor in the saddle point differs from that in the ground state [27]. This is known to be of particular importance when examining the stress-induced preferred absorption effect [36]. In practice, the resultant equations do not admit closed-form solutions such that expressions to estimate the dislocation bias have assumed—either implicitly or explicitly—that the ground and saddle-point configurations have identical isotropic dipole tensors and that the diffusivity is isotropic [15,37–40]. In this case, the dipole tensor can be characterized solely in terms of the relaxation volume ΔV. Generally, the relaxation volume is defined through the material compliance as

$$\Delta V = S_{iikl}p_{kl}, \tag{4}$$

to which both isotropic and anisotropic parts of p can contribute [41]. To ease comparison with conventional bias estimates, we write

$$p_{ij} = K \, \Delta V \, \delta_{ij} + \tilde{p}_{ij}, \tag{5}$$

where the tensor $\tilde{p}$ is assumed to be zero in the analytical expressions for bias. A comprehensive study in aluminum highlighted the effects of $\tilde{p}$, demonstrating the consequences of its components for both the ground and the saddle-point configurations when considering the isolated dislocation [42]. This is capable of changing the apparent bias of isolated dislocations but can also impact the effect of configuration through the interactions between dislocation strain fields not captured in the relaxation volume. However, for this paper, we will neglect the possible influence of such components such that our findings can be compared directly to the conventional analytical expressions and provide a direct assessment of the impact of dislocation configuration on sink strength and bias.

A. Sink strength calculations

Sink strengths are calculated by solving Eq. (1) around a particular instance of a sink, computing the net point defect current I into that sink, and then equating the the total rate of defect loss to some homogenized absorbing medium. That is, one writes

$$I = \oint_A \mathbf{J} \cdot dA, \tag{6}$$

over the surface A of a given sink with $\mathbf{J}$ given by Eq. (2) and then finds the appropriate sink strength k^2 in the corresponding homogenized medium as

$$Dk^2 C = I\rho_{\text{sink}}, \tag{7}$$

where ρ_{sink} is the sink density and C is the mean-field concentration of defect n.

Different authors often use different boundary conditions when determining the current I and consequently derive different solutions for k^2. The most common assumption is that one can draw a cell around a given defect (a cylinder for dislocations) sized to the mean defect spacing and set the concentration at the boundary of that cell to the mean-field value. That is, one solves

$$-\boldsymbol{\nabla} \cdot \mathbf{J} + g = 0, \tag{8}$$

$$c(r_0) = 0, \tag{9}$$

$$c(R) = C, \tag{10}$$
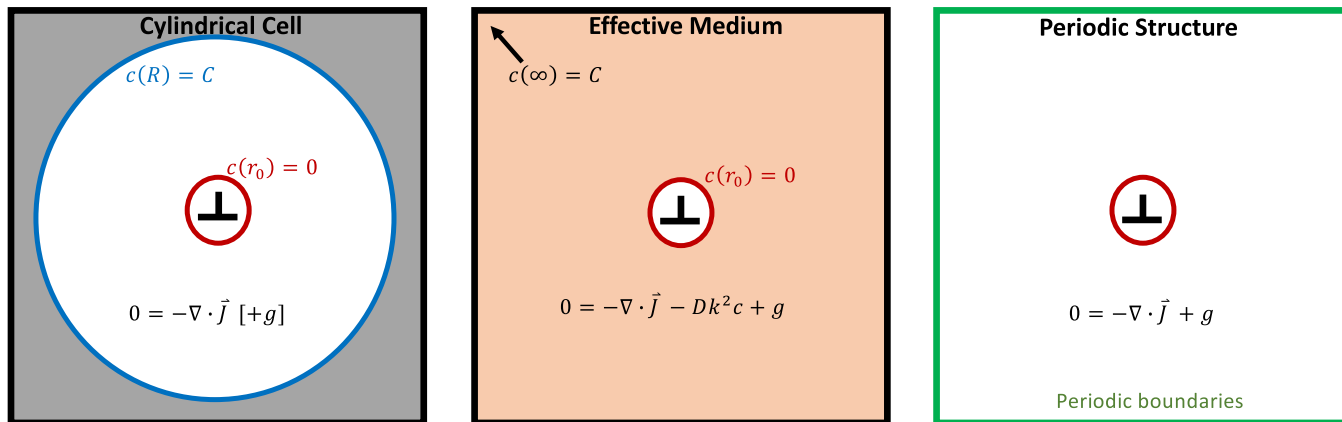
FIG. 1. Schematic of the approaches used to calculate sink strengths. In this paper, the analytical estimates produced from both the cylindrical cell and the effective medium approaches are compared to numerical calculations for various periodic structures.

where r_0 is a capture radius and R is an outer cell radius corresponding to the sink density. We will refer to the sink strengths derived in this manner as the Laplace cell estimate when the source terms are neglected and the Poisson cell estimate when they are included.

It has been pointed out by Brailsford and Bullough that, although the above approach is likely accurate to first order, it is not internally consistent [14] in the sense that the mean concentration and the appropriate representative concentration at the surface of the cylindrical cell are not the same. They propose an alternative means of homogenization to avoid this subtlety. This "effective medium approach" involves embedding the sink directly in the homogeneous absorbing medium created by all the other sinks k_{tot}^2 and solving instead

$$-\nabla \cdot \mathbf{J} + g - Dk_{\mathrm{tot}}^2 c = 0, \tag{11}$$

$$c(A) = 0, \tag{12}$$

$$c(\mathbf{r} = \infty) = C = g\left(Dk_{\mathrm{tot}}^2\right)^{-1}, \tag{13}$$

where the final boundary condition indicates that the flux vanishes infinitely far from the sink. Although this procedure describes the mean concentration consistently by definition, analytical solutions are often unavailable or complex, and numerical solutions are unavailable due to its nature.

Neither condition above is satisfactory for the curved, noninfinite, or otherwise nonideal geometries associated with realistic dislocation networks. As such, we consider a third scenario in which periodic boundary conditions are employed. In this case, the net current into the sink (or sinks) in the box will be equivalent to the net source rate $I = gV$ at steady state by definition. Instead, all that remains is to relate the mean concentration in the system to the sink strength that is

$$-\nabla \cdot \mathbf{J} + g = 0,$$

$$c(r_0) = 0,$$

$$\int Dk^2 c \, dV = gV. \tag{14}$$

This approach also self-consistently relates mean concentration to sink strength, whereas allowing multiple sinks in

various spatial configurations to be analyzed. A schematic comparing the three approaches is shown in Fig. 1, noting that the closed-form expressions to which we will later compare have been derived in the first or second condition, whereas the numerical calculations in this paper are all performed in the third.

B. Local absorbing medium

Perhaps, the most direct approach to solving the set of Eqs. (14) would be to craft a finite element mesh which explicitly resolves the core of each dislocation. However, the core radius is on the order of a few atomic spacings, and the size of the periodic volume required to sample a statistically significant number of dislocations can span several microns depending on the density. Accordingly, it is preferable to avoid such explicit resolution requirements if possible and instead use an approach that allows the sinks to be described discretely but does not require the core to be resolved. To this effect, we use the recently introduced local absorbing medium (LAM) approach [29].

This methodology leverages the same techniques used to determine sink strengths for a homogeneous system [e.g., the approach of Eqs. (6) and (7)] and applies them to a finer volume corresponding to particular sinks. That is, instead of

$$\frac{dc}{dt} = -\nabla \cdot \mathbf{J} + g - Dk^2 c, \tag{15}$$

with a uniform and universal absorbing medium k^2, one writes

$$\frac{dc}{dt} = -\nabla \cdot \mathbf{J} + g - Ds(\mathbf{r})c, \tag{16}$$

where $s(\mathbf{r})$ describes the strength of an absorbing medium but varies spatially and is only nonzero in the immediate vicinity of a sink. The appropriate magnitude of s is determined by bounding the volume over which the medium will be distributed and demanding that the same flux cross that boundary when the resolved sink is replaced with the absorber as described in the Appendix. This quantity is determined uniquely through the geometry of the sink, the strain fields, and the volume over which the absorber becomes distributed and is
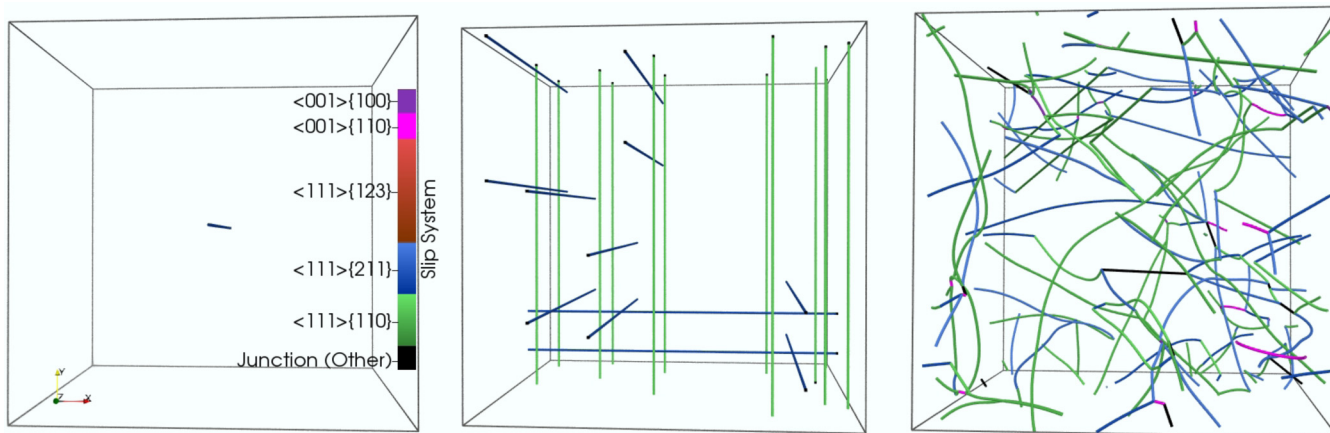
FIG. 2. Examples of the three types of dislocation configuration considered in this paper, including a periodic 2D array (left), a 3D array of randomly placed dipoles (center), and a complex 3D network generated using DDD (right).

independent from values of the point defect concentration in the bulk.

C. Dislocation configurations

This paper includes three types of periodic dislocation microstructure, each generated in α-Fe, as illustrated in Fig. 2 with the densities that span the range of 5×10^{12} to 10^{15} m^{-2}. The first set is a periodic array of infinite pure edge dislocations, designed to most closely replicate the two-dimensional closed-form expressions for sink strength and bias generated in cylindrical cells. For these calculations, the density is varied simply by scaling the box size with a single dislocation at the center of the box for each case. The second is a randomly generated array of dipoles. For these calculations, the [111] crystallographic direction is oriented along the x basis such that pure edge dislocations can be inserted with line directions lying along z or y, and pure screw dislocations can be placed lying along x. The ratio of edge to total dislocation content varies randomly between 0 and 1 for each instantiation of the random array. A discrete set of box sizes is used with additional variation in density accessed by changing the number of dislocations in the box. Finally, we consider complex dislocation networks generated from the dynamic capabilities of the DDD approach.

Existing DDD simulation methods are also used to generate the strain fields associated with each of the configurations considered in this paper. In particular, the variant of a mechanical solver which uses a fast Fourier-transform (FFT) approach within the discrete-continuous model framework (DDD-FFT) [43–46] has proven particularly efficient for our purposes. This technique produces each component of the elastic strain tensor at regular intervals on a Cartesian grid throughout the material. For each type of microstructure, the dislocations are placed within the DDD-FFT simulation volume, the corresponding strain fields are generated, and the appropriate LAM are assigned to each segment. Finally, Eq. (1) is solved for the steady-state defect concentration using finite differences on the same grid at which the strain values are known and used to determine the sink strength. This final step is repeated for defects of various relaxation

volumes. For the maximal symmetry case of the periodic array, the calculations were repeated outside of the DDD-FFT framework and without the LAM (for validation purposes) using a high-resolution 2D grid with a resolved boundary for the dislocation core and a strain field generated from the superposition of the isolated edge dislocation solution. In all cases, the material properties considered correspond to an isotropic analog of α-Fe as shown in Table I, and the nominal temperature used in these calculations was near the peak void swelling temperature of bcc iron and ferritic steels [47,48]. The complex networks are created by placing an initial dislocation population of loops with random positions and sizes in a simulation box. These loops are randomly distributed among the possible variants of the $\langle 111 \rangle \{110\}$ and $\langle 111 \rangle \{112\}$ slip systems. These seed loops may be of either pure edge (prismatic) or varying edge-screw (glide) character, although, in both cases, the loops are glissile within the relevant slip systems. The system is then loaded under intense stresses on the order of a few gigapascals to activate growth of glide loops and the operation of prismatic loops as Frank-Reed sources. The resulting interactions between the loops leads to the formation of a network. Several hundred steps of such loading are followed by 20 000 steps of relaxation, a duration sufficient to remove any unstable glide loops which

TABLE I. Standard parameters used in this paper, designed to emulate α-Fe.

Parameter	Value	
K	270 GPa	
ν	0.29	
T	675 K	
b	0.25 nm	
Slip mode	B ($\times 10^{-5}$ Pa s)	τ_c (MPa)
$\langle 111 \rangle \{112\}$	8	10
$\langle 111 \rangle \{112\}$	8	10
$\langle 111 \rangle \{123\}$	8	10
$\langle 001 \rangle \{110\}$	80	300
$\langle 001 \rangle \{100\}$	9000	300

Size (nm)	1440	720	360
Grid points	128	64	64
Mesh spacing (nm)	11.25	11.25	5.63
$\rho_{\min}$ (10^{13} m^{-2})	0.5	2	8
$\rho_{\max}$ (10^{14} m^{-2})	4	4	16

might remain in the structure. This process leaves a tangled network consisting of segments inhabiting the original set of slip systems, segments which have cross slipped to new systems and remained there, and junctions formed during the loading and relaxation process. During both processes, dislocation velocities are computed from the resolved stress τ through an overdamped equation of motion,

$$v = \frac{\max(\tau - \tau_c, 0)}{B}, \tag{17}$$

using drag coefficient B and Peierls stress τ_c parameters which reproduce atomistic simulations of dislocation interactions to acceptable accuracy [12].

To properly distinguish the highly ordered periodic array for the other two configurations which are designed to target less ordered structures, a certain dislocation density must be maintained in the simulation volume. As the number of dislocations in the box drops, the full system becomes increasingly ordered through the periodic images, and the mean spacing between dislocations should be small compared to the box size for the periodic system to reflect significant disorder. As a guiding rule, we use

$$\rho_{\min} \simeq n_0 L^{-2} \tag{18}$$

for box size L where n_0 is approximately 20 to avoid periodicity concerns. Conversely, the assumptions behind the LAM begin to break down where the absorbing regions begin to overlap significantly. This can be expected to occur wherever the mean spacing between dislocations approaches a few mesh spacings, that is, to say,

$$\rho_{\max} \simeq \frac{1}{\pi} \left(\frac{n_{pt}}{n_{\text{sep}} L} \right)^2, \tag{19}$$

where n_{pt} is the number of mesh points, n_{sep} is the minimum acceptable average spacing, and certainly no fewer than 2 but more reasonably nearer to 6. The boxes sizes considered here and target density ranges are shown in Table II. Due to the nature of the microstructure generation process outlined above, the density of the complex networks in a quasirelaxed state cannot be controlled with precision, however, these ranges were used to inform the target density range to be considered for each simulation volume.

III. RESULTS

For each of the three types of dislocation structure, the sink strength is computed both with and without the effect of strain field interactions on point defect diffusion. For the periodic array, only one calculation was required at each density. For the more complex structures (the random 3D arrays and the networks), multiple calculations were performed at each density to sample the variety of structures available. In each case, 50 independent arrays were considered. Three successive box sizes (0.36, 0.72, and 1.44 microns) were used to span the array of dislocation densities required with between 6 and 96 dipoles in each box for the random arrays. In some cases, the same density was sampled at multiple box sizes for intermediate densities to assess any effect of the system volume. The analysis is simplified by introducing the capture efficiency Z, which gives a dimensionless measure of sink strength, and for dislocations,

$$Z = \frac{k^2}{\rho_d}, \tag{20}$$

where ρ_d is the dislocation density.

A. Sink strengths without strain effects

First, each configuration was analyzed for noninteracting defects ($p_{ij} = 0$) and compared to the corresponding analytical estimates for sink strength derived from the cylindrical cell and effective medium approaches. In the absence of strain interactions, the cylindrical cell approach gives the estimate widely applied to dislocation climb kinetics [49–51],

$$Z_\ell = \frac{2\pi}{\ln R/r_0} \tag{21}$$

without considering source terms (the Laplace solution). It gives a slightly higher value,

$$Z_p = \frac{2\pi}{\ln R/r_0 - \frac{1}{2}\left(1 - \frac{r_0^2}{R^2}\right)}, \tag{22}$$

when source terms are included (the Poisson solution) where the outer cell radius R is related to the dislocation density as $R = (\pi \rho_d)^{-1/2}$ in both cases. The effective medium approach gives a more complicated result (the embedded solution),

$$Z_{\text{em}} = \frac{2\pi k r_0 K_1(k r_0)}{K_0(k r_0)}, \tag{23}$$

where K is the modified Bessel function of the second kind. This is rarely used, likely due to its transcendental nature as $k = \sqrt{Z\rho}$. For the physically relevant case of $k r_0 \ll 1$ (that is, the dislocations are separated by more than the core radius on average), this reduces to the slightly more tractable but still transcendental expression,

$$Z_{\text{em}} = \frac{2\pi}{K_0(k r_0)}. \tag{24}$$

For the periodic array, the sink strengths found from the DDD-FFT and the 2D resolved boundary numerical solutions matched each other to within 1% across the entire range of density and were slightly higher than the Poisson estimate which can be seen in Fig. 3. This is in agreement with previous calculations examining such configurations with a kinetic Monte Carlo approach [52].

The sink strengths of the other configurations, however, differed substantially from this estimate. For random assignments of dipoles, the sink strength was significantly lower on average. There was some degree of variation between instances of the dipole arrays, demonstrated in Fig. 4 where
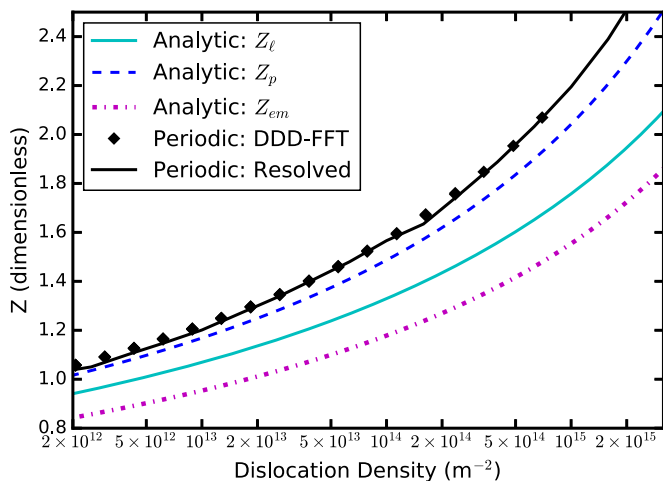
FIG. 3. The dislocation sink strength of a periodic array of infinite straight dislocations, The solution from the DDD-FFT code with local absorbing media is compared to a high-resolution numerical solution with the boundary condition enforced directly at the dislocation core. The predictions based on the Laplace and Poisson solutions in a cylindrical cell as well as a dislocation embedded in an equivalent effective medium are also shown.

the median, interquartile, and full range are shown for arrays at a variety of densities. For a given density, the configuration with fewer dislocations in the box (that is, to say, the smaller sample volume) resulted in a somewhat higher median sink strength, which appears consistent with the findings for the single dislocation configurations. Indeed, if the number were reduced to 1, the periodic array would be restored with its significantly increased sink strength. The reduction in median sink strength that occurs by increasing the sample volume and reducing the periodicity of the system appears to saturate relatively quickly, however, and statistically significant
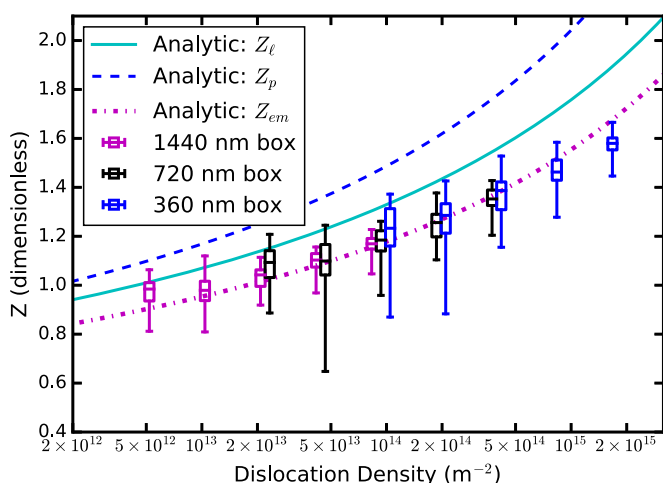
FIG. 4. The dislocation sink strength of an array of randomly inserted infinite dipoles. Simulations were run in each three different volumes, each sampling five unique densities. For each case, the median of 50 randomly generated instances is shown along the with the interquartile and full ranges and compared against the three analytical expressions.
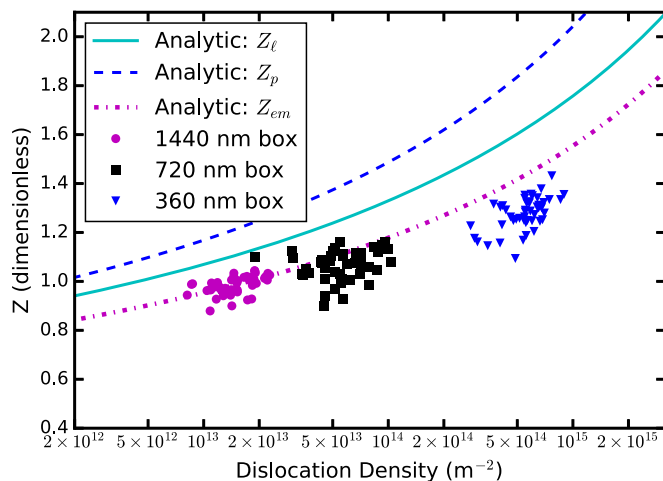
FIG. 5. The dislocation sink strength of dislocation networks in iron. Each of the 48 microstructures for each box size is shown as a unique data point and compared to the analytical predictions of sink strength based on simplified boundary conditions.

differences are really only observed for the simulations with the minimum number of dipoles. As the volume converged on representative sizes, the sink strength of these random arrays approached the effective medium solution given by Eq. (24).

The capture efficiencies of the complex networks (excluding strain interactions) are shown in Fig. 5. For each volume, between 40 and 50 instances were examined. The sink strengths of these networks sit near, if slightly below, that of the random dipole arrays. The variability in capture efficiency also appears largely comparable to that seen for random dipoles. The sink strength that emerges from these configurations—presumably closest to the microstructure of a real metal—sits only slightly below the effective medium estimate of the capture efficiency, indicating that the use of this value to describe the overall homogenized capture behavior of three-dimensional networks is likely appropriate. However, the strain field interactions with the point defects can significantly increase the sink strength from these estimates, and this effect is examined in the next section.

B. Strain field interactions

In addition to examining the sink strength of noninteracting defects, each of the configurations generated above was considered for interacting defects with different magnitudes of relaxation volume. These spanned roughly 0.1–1.7 atomic volumes and include the ground-state relaxation volumes of the vacancy and self-interstitial atom (SIA) computed from an empirical potential common for radiation damage in bcc Fe [53]. Closed-form analytical solutions for the isolated cylinder problem are also available in the case of an isotropic point defect interacting with an edge dislocation in an isotropically elastic medium and follow:

$$Z_\ell(L) = \frac{2\pi I_0(L/2r_0)}{K_0(L/2R)I_0(L/2r_0) - K_0(L/2r_0)I_0(L/2R)}, \quad (25)$$

where I and K are the modified Bessel functions of the first and second kinds, noting that several sightly different but similar variants exist depending on the boundary conditions
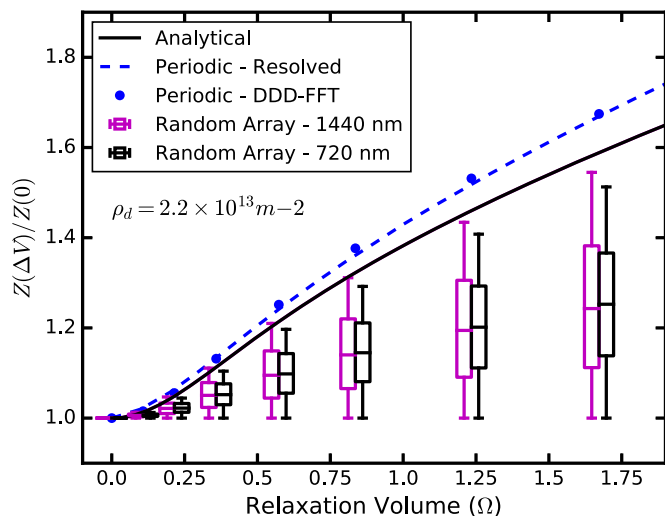
FIG. 6. The increase in sink strength due to strain field interactions with the point defect as a function of relaxation volume. Simulations for regular periodic arrays and randomly placed dipole configurations are shown alongside the predicted effect based on Eq. (25).

FIG. 7. The increase in sink strength for dipole arrays due to strain field interactions as a function of the edge content of the system. The predicted bias based on the analytical expressions of Eq. (27) (solid lines) are contrasted with the realized values for particular arrays (points) and a least-squares fit to that data (dashed lines).

enforced [37–39]. The point defect and elastic properties enter through the interaction distance L, given by

$$L(\Delta V, b) = \frac{Kb|\Delta V|}{2\pi k_b T} \frac{1 - 2\nu}{1 - \nu}, \qquad (26)$$

which also depends on temperature. Note that reversing the sign of the relaxation volume creates a symmetric image in the interaction energy around an edge dislocation such that only the magnitude impacts Eq. (25). When considering strain interactions, the effective medium approach does not admit an exact closed form solution, a point we will revisit in the next section.

As shown in the previous section, the sink strength for the configurations we examine here differs—even in the absence of strain interactions—from analytical predictions based on such cylindrical cell approximations. Consequently, Z values from this expression are difficult to compare directly to the realized capture efficiency of any given three-dimensional system. To more directly quantify the strain field effect on kinetics, we will work with a normalized capture efficiency $Z(\Delta V)/Z(0)$ rather than the capture efficiency directly. Figure 6 shows the effect of strain for both of the straight dislocation configurations. As with the base sink strength, the DDD-FFT implementation with local absorbers can be compared directly to a 2D mesh with an explicitly resolved dislocation core, and both calculation approaches are included. The fully periodic array demonstrates a slight increase in the strain effect when compared to Eq. (25), whereas the random dipole arrays demonstrate a substantially reduced effect on average. Some of the reduction is attributable to the presence of screw character dislocations in these simulations, and indeed the configurations which were entirely screw produced no increase in the capture efficiency. However, the configurations which were entirely edge still showed somewhat lower capture efficiencies than would be expected from Eq. (25) at large values of the relaxation volume. Although the data shown is
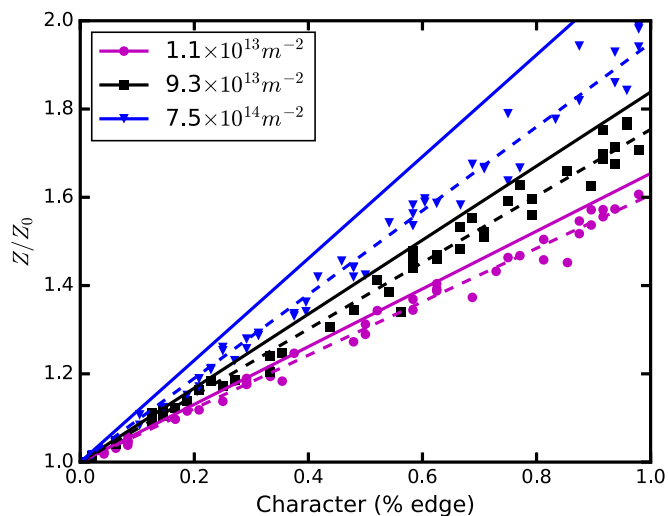
for a density of 2×10^{13} m^{-2}, such an effect was observed consistently across box sizes and densities.

Dislocations of purely screw character produce no dilatation in a medium with isotropic elasticity. The random dipole arrays are oriented such that the dislocations all have either pure edge or pure screw character. Accordingly, one might expect that the wide range of biases evident in these calculations are solely a consequence of the fraction of dipoles that happen to take the screw orientation when the array is constructed. Consider a modification of the bias according to

$$Z^{\text{ad}}(\Delta V, \rho) = Z_0(\rho) + \chi \{[Z(\Delta V, \rho)] - Z_0(\rho)\}, \qquad (27)$$

with χ as the fraction of dipoles inserted with edge character, Z given by Eq. (25), and Z_0 given by Eq. (21). We will refer to this as the character adjusted character prediction. Figure 7 compares the bias of each array as realized from three-dimensional calculations to the analytically predicted values adjusted for the character of each array. Three representative densities are shown, and in each case, the linear increase in bias with edge content is followed broadly but imprecisely. Significant deviation in the capture efficiency is still observed, and the analytical values generally overpredict the acceleration in capture kinetics.

For the complex networks, it is somewhat more difficult to analyze the effect of strain on capture kinetics due to the variation in density between each instantiation of the dislocation microstructure. It is not possible to directly examine the effect of relaxation volume and network character at a fixed density as no concrete reference density is available for these simulations. Instead, we show $Z(\Delta V)/Z_0$ as a function of density for two selected values of the relaxation volume in Fig. 8 as well as the corresponding predictions of Eq. (25). The systematic overprediction supplied by the analytical formula is expected given the effect of screw dislocations in dipole case, but it is
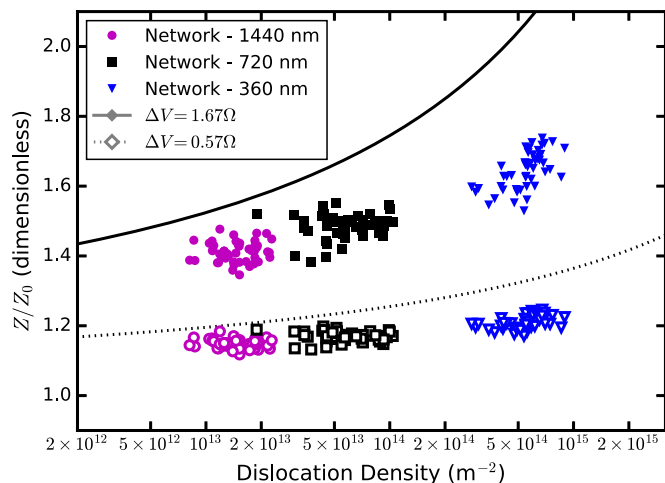
FIG. 8. The increase in sink strength due to elastic interactions with complex networks. Equation (25) is compared to numerical calculations for defects with large (solid line, filled points) and intermediate (dotted line, open points) values of the defect relaxation volume.

FIG. 9. The deviation of dislocation network capture efficiencies from the predictions of analytical expressions. The top plot reflects the predictions of the cylindrical cell approach Z_ℓ without adjusting for network character. The center plot uses Z_ℓ but includes the character adjustment. The final plot uses the surrogate sink strength described by Eq. (30).

not evident what role is played by configuration of the network (that is, spatial correlation, ordering, etc.).

Addressing the effect of configuration requires an alternative to the analytical expressions for the pure edge case, and accordingly, we propose a surrogate expression of the following form:

$$Z_{\text{fit}}(\delta) = \frac{2\pi}{\ln(R/\delta)}\left(A_0 + A_1\frac{r_0}{R} + A_2\frac{\delta - r_0}{R}\right), \quad (28)$$

where δ constitutes an effective capture distance,

$$\delta = \sqrt{r_0^2 + L^2/4} \quad (29)$$

containing the point defect properties, material elastic constants, and temperature. This approach is motivated by prior approximations of the sink strength [40,54] but includes fitting parameters A_0, A_1, and A_2 which provide corrections for spatial correlation effects. The first accounts for systematic deviation due to collective effects, the second describes how this changes with density, and the third describes how collective effects scale with interaction strength. Together, these can accommodate differences in sink strength due to ordering and structure. We also note that the strain-free capture distance r_0 is physically difficult to define but is usually assumed to be one to two lattice units and becomes important only for very weak interactions where L is comparable or shorter.

When combined with a linear dependence on edge content per Eq. (27), a complete expression for sink strength can be established

$$Z_{\text{fit}}^{\text{ad}}(\chi, \delta)$$
$$= \frac{2\pi}{\ln R/r_0}\left(A_0 + A_1\frac{r_0}{R}\right)$$
$$\times \left[1 + \chi\left(\frac{\ln R/r_0}{\ln R/\delta}\frac{A_0R + A_1\delta + A_2(\delta - r_0)}{A_0R + A_1r_0} - 1\right)\right], \quad (30)$$

which can incorporate the effects of character (edge vs screw) and structure (order vs disorder) on sink strength separately. However, the edge character of the networks is somewhat more complex to quantify due to the presence of mixed character segments and junctions. We will use

$$\chi = \frac{\sum_i |\mathbf{b}_i \times \ell_i|}{b\sum_i |\ell_i|}, \quad (31)$$

where $\mathbf{b}_i$ is the Burgers vector of the ith segment, ℓ_i is the line connecting its end points, and b is the magnitude of the Burgers vector used in connection with Eq. (26). This gives the ratio of Burgers vector components lying in the edge direction to the reference magnitude and can conceivably exceed unity for networks with significant junction content. The χ used for the simpler case of dipole arrays is a degenerate form of this expression when neither junctions nor mixed character segments are present in the network.

To quantify the effectiveness of this approach on a case-by-case basis, consider the error,

$$\eta_Z = \frac{Z - Z^*}{Z}, \quad (32)$$

where Z^* represents the predicted capture efficiency, and Z represents the measured capture efficiency of a given microstructure instantiation as found from the DDD-FFT/LAM approach. The performance of the analytical expression Z_ℓ given by Eq. (25) is shown in Fig. 9 as well as an adjustment for network character Z_ℓ^{ad} per Eq. (27). This is compared against the surrogate expression $Z_{\text{fit}}^{\text{ad}}$, which considers both

TABLE III. Coefficients to calibrate the capture efficiency for different types of dislocation structure.

Structure	A_0	A_1	A_2
Periodic array	1.14	2.81	0.64
Random dipole	0.91	−2.16	−0.92
Full network	0.87	−5.12	−0.77

structure and character, Eq. (30). The statistical distribution of errors in each case is represented via median, interquartile, and full range values for each of several relaxation volumes with the box size serving as a rough measure of the dislocation density. Both of the predictions based on Eq. (25) show a pronounced systematic error in Z. The overprediction worsens with increasing density or interaction strength, which is mitigated but not eliminated by adjusting for network character. A fit of the surrogate expression to the dislocation network database describes each set to within the inherent statistical spread, which stands between ± 5 and $\pm 15\%$ depending on the size of the system. A least-squares analysis was applied to the databases for each of the three configuration types (periodic 2D array, random dipoles, and complex network), generating the coefficients in Table III.

IV. DISCUSSION

The effect of strain on capture efficiency factors prominently in the driving force for void swelling through the dislocation bias, which motivates excess vacancy flux. Here, we adopt the convention,

$$B_d = \frac{Z_i}{Z_v} - 1, \tag{33}$$

where Z_i and Z_v reference the capture efficiency for SIA and vacancy defects, respectively. As the bias is a ratio of Z, errors which are *systematic* (e.g., the coefficient A_0 in the previous section) will have no effect, whereas errors that scale with interaction strength (described by A_2) will. The key question is whether effects on sink strength produced by structure (order vs disorder) and character (edge vs screw) are systematic in nature or not. The bias analysis here is targeted to ferritic/martensitic (F/M) steels with the vacancy relaxation volume, dislocation density, and temperature of interest set accordingly. The parameters for this system are not anomalous, however, and fall within the ranges for typical metals where the vacancy defect relaxation volume is less than a third of the atomic volume whereas the SIA can vary from roughly one to two atomic volumes [41,55].

Bias factors have been generated from the surrogate sink strength in Eq. (30) for all three configurations considered in this paper and are compared against the conventional analytic expression in Fig. 10. No notable difference between the dipole array and the network configurations appears through the range of SIA interaction strengths examined. The highly ordered 2D system displays higher biases than the other two configuration types, and all have departed significantly from the conventional expression within the plausible range of SIA relaxation volumes. The impact of screw character segments is evident even for weak interactions, and the bias is also shown
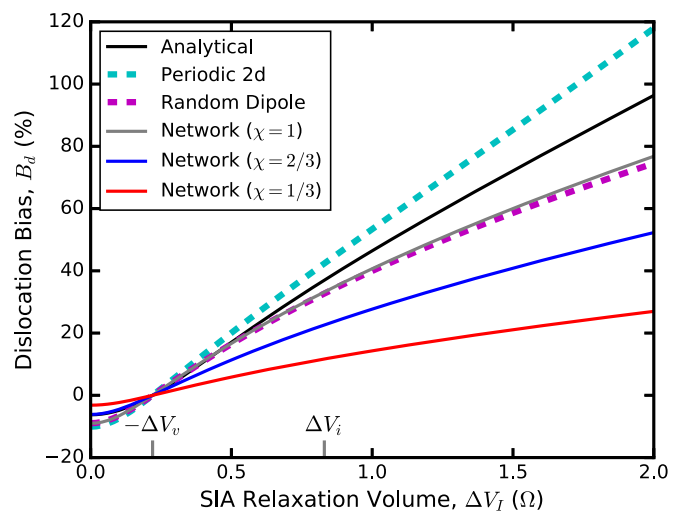
FIG. 10. The dislocation bias factor B_d as a function of SIA relaxation volume at a density of 3×10^{14} m^{-2} and the nominal defect relaxation volumes for Fe marked. The conventional analytical expression is shown directly as well as the surrogate sink strength expression representing the three dislocation structures considered in this paper. For the network case, three distinct values of the character parameter are considered.

for networks which are 1/3 and 2/3 screw. The roughly linear scaling of the dislocation bias with edge content is not surprising or counterintuitive, but the mesoscale approach taken here confirms that it functions effectively for realistic networks. The reduction of bias for each 1/3 increment in screw content is of similar magnitude to the effect of configuration, suggesting both factors contribute in real material systems. The range of possible configurations has not been fully explored in this paper, however, and nonuniformity within the network can only be expected to increase for engineering materials (for instance, in a cell-wall-type dislocation microstructure), which intuitively suggests that further decrease in bias is possible for such cases.

Together, these factors can help explain the low swelling rates in ferritic materials where empirical estimates of the bias factor range from fractions of a percent to low single digits [56]. The maximum achievable steady-state swelling rate relative to radiation dose measured in displacements per atom (dpa) is approximately [57]

$$S \approx \frac{\epsilon B_d}{4} \ (\%/\text{dpa}), \tag{34}$$

where ϵ is the point defect survival fraction—a material- and irradiation-condition-dependent consequence of cascade structure—usually between 10 and 30% [58–60]. Accordingly, the conventional expression suggests peak swelling rates between 1%/dpa and 3%/dpa if the survival efficiency is included and nearly 10% if it is neglected. Notably, recent *ab initio* calculations suggest a larger intersitital relaxation volume of roughly 1.6 Ω in both the ground-state and the saddle-point configurations, which would correspond to still higher swelling rates [61]. The highest measured swelling rates for these materials are reported for FeCr binary alloys and α-Fe not exceeding 0.2% in the former [47,48,62] but

possibly as rapid as 0.5% for the latter (in cold-worked metal) with shorter incubation periods [47,56]. Alloys featuring a martensitic microstructure exhibit even lower swelling rates [63,64], generally attributed to high densities of lathe boundaries and precipitates that can act as alternative sinks and recombination centers, frustrating the conditions which led to Eq. (34). In F/M steels, the networks strongly favor the screw configuration in both the unirradiated and the irradiated conditions, suggesting 20% is a reasonable estimate for χ [65,66] in which case the present paper predicts a bias near 8% and a peak steady-state swelling rate between 0.2%/dpa and 0.6%/dpa.

Several additional factors may influence the sink efficiencies reported here. Notably, isotropic assumptions are taken throughout this paper in regard to both the bulk diffusivity and the defect dipole tensors. Anisotropy in either may have significant effects on defect capture, potentially modifying the capture efficiency of dislocations directly. Furthermore, both contribute to a change in the sink strength of a dislocation with applied stress, a phenomenon which does not occur with isotropic considerations. Consequently, one expects additional collective effects when anisotropy becomes important as the local stress state created by neighboring dislocations can be expected to join defect depletion in contributing to changes in the sink strength. This can induce further deviation in mean behavior from the analytical expressions but perhaps more importantly induce additional variance in bias from instance to instance on the micron scale. Finally, point defect clusters are also produced in significant quantities in most irradiation conditions and have different dipole tensors from their monodefect counterparts. Whereas this does not affect the sink efficiency of the point defects themselves, it may change the overall interstitial bias (as plotted in Fig. 10). We note that the present approach can be extended directly to determine the sink strengths of sufficiently small clusters provided the dipole tensors are known, whereas the DDD framework offers the potential to assess average lifetimes of larger glissile clusters by treating them explicitly as prismatic dislocation loops.

Finally, we turn our attention to the growth of prismatic dislocation loops in irradiated metals. In the homogenized interpretation, interstitial-type loops will grow and vacancy-type loops will shrink if the loop bias factor exceeds the network bias factor. The opposite occurs in the case where the loop bias falls below the network, and, in either case, the size distribution broadens over time. Bias factors for loops are more difficult to generate analytically, and different approaches have produced loop capture efficiencies that agree only in the sense of a complex nonmonotonic dependence on the size of the loop and the total dislocation density [67,68]. Consider a further complication: That, for any given loop, the capture kinetics will depend on where it is positioned in regard to the surrounding network and other loops. The capture efficiencies seen in this paper can vary by as much as 10% for volumes on the order of a cubic micron. At the 10-nm length scale relevant to irradiation induced prismatic loops, the variations in defect supersaturation are significantly more pronounced. This produces locations in the microstructure where loop nucleation and growth is encouraged and others where it is frustrated, influencing the locations where such

loops will appear. It is not at all clear that mean-field quantities, such as the average point defect concentrations or the capture efficiencies in a homogenized system enter into this picture when loops are distributed such that the environment they see is not representative of such system averages.

V. CONCLUSIONS

The configuration of a dislocation network influences the capture kinetics of point defects in the system with the sink strength of a purely periodic system exceeding that of more realistic 3D configurations by a factor of as much as 2. When strain field interactions are neglected, the effective medium approach provides the most representative description of sink strengths for realistic three-dimensional dislocation networks. Whereas this approach provides a reliable estimate of the average sink strength of networks, individual instantiations at similar densities follow a statistical distribution such that the sink strength could differ between instances by as much as 30%, depending on the size of the system. Local variations are even stronger, and the point defect supersaturations vary widely from point to point within the material volume, potentially driving the kinetics of both loop and void nucleations away from estimates based on mean-field quantities.

The effect of strain field interactions on the dislocation structure also vary from configuration to configuration. The nature of the network in terms edge, screw, and junction content strongly influences the dislocation bias. Accounting for network character with a fairly straightforward quantification of the edge dislocation content produces sink strength estimates nearer to the capture kinetics realized in the DDD calculations. However, screw and mixed character segments do not account entirely for the difference between the analytically predicted sink strengths and the sink strengths of realistic dislocation networks. The additional discrepancies are due to the irregular structure of the networks for which the effective medium boundary conditions provide an acceptable description of these configurational effects without strain but do not yield a compact solution when energetic interactions are considered. Instead, we have introduced a fitted expression which describes the realized mean sink strengths of DDD microstructures over the physically relevant range of interaction strengths and dislocation densities. This approach implies a dislocation bias factor for F/M steels and FeCr binary alloys much more consistent with the swelling rates observed in those material systems.

APPENDIX: SINK REGULARIZATION

Dislocation sinks are regularized to the FFT grid using the local absorbing medium approach. Within this framework, each segment is distributed to the neighboring grid points as a diffuse absorbing medium in such a manner as to reproduce the defect absorption rates of the discrete sink. This is accomplished via the following conceptual procedure:

(1) Consider a cylindrical volume of radius r_A containing the segment.

(2) Assign a radially dependent absorption density $s(r)$ within this volume.

(3) Choose the form and magnitude of $s(r)$ such that neither the concentration at nor the flux across the surface of the cylinder is modified if the discrete sink is replaced with the absorbing medium.

(4) Assign a discrete absorption coefficient s^i to each grid point, which is the average s within the associated volume.

The appropriate values of $s(r)$ follow from preserving the flux across the medium boundary. To this end, consider a dimensionless flux at the absorber boundary r_A,

$$\phi = \frac{r_A c'(r_A)}{c(r_A)}, \quad (A1)$$

which must be identical if the inner boundary condition is replaced by the absorber $s(r)$. In cylindrical coordinates, this condition can be satisfied if the absorber takes the form

$$s(r) = \frac{\phi}{r_A}\left(\frac{1}{r} + \frac{\phi}{r_A}\right) + \beta \nabla^2 E. \quad (A2)$$

In the case without strain, $c(r)$ is given by

$$c(r) = \frac{c(r_A) \ln r/r_0}{\ln r_A/r_0}, \quad (A3)$$

and ϕ becomes

$$\phi = 1/\ln r_A/r_0. \quad (A4)$$

A power-law interaction potential of the form $\beta E(r) = a_0 r^n$ gives a radial defect profile of

$$c(r) = c(r_A) \exp\left(a_0 r_A^n - a_0 r^n\right)\left(\frac{E_I a_0 r^n - E_I a_0 r_0^n}{E_I a_0 r_A^n - E_I a_0 r_0^n}\right), \quad (A5)$$

where E_I is the exponential integral and

$$\phi = n\left(\frac{\exp a_0 r^n}{E_I a_0 r_A^n - E_I a_0 r_0^n} - a_0 r^n\right). \quad (A6)$$

In the case where $E(r)$ has strong angular dependence or no analytic expression for E is available, an effective radial potential can be determined by an exponential averaging procedure,

$$\exp\left[-\beta U(r)/2\right] = \frac{1}{2\pi} \int_0^{2\pi} \exp\left[-\beta E(r,\theta)/2\right] d\theta, \quad (A7)$$

which has been shown to adequately represent the net flux [69,70]. We note that, although the Laplacian of E vanishes analytically for harmonic interactions, such as those which appear in this paper, it appears numerically due to finite difference discretization and in such cases significantly influences the appropriate absorber distribution. A full description and validation of this procedure is available, including in conditions with multiple dislocations [29].

[1] V. Sears, J. Nucl. Mater. **39**, 18 (1971).

[2] A. Brailsford, R. Bullough, and M. Hayns, J. Nucl. Mater. **60**, 246 (1976).

[3] P. T. Heald and M. V. Speight, Philos. Mag. **30**, 869 (1974).

[4] M. F. Wehner and W. G. Wolfer, Philos. Mag. A **52**, 189 (1985).

[5] T. Okita and W. Wolfer, J. Nucl. Mater. **327**, 130 (2004).

[6] P. T. Heald and M. V. Speight, Philos. Mag. **29**, 1075 (1974).

[7] J. Matthews and M. Finnis, J. Nucl. Mater. **159**, 257 (1988).

[8] R. Bullough and M. H. Wood, J. Nucl. Mater. **90**, 1 (1980).

[9] E. Savino and C. Tome, J. Nucl. Mater. **108–109**, 405 (1982).

[10] R. Schäublin and Y. Chiu, J. Nucl. Mater. **362**, 152 (2007).

[11] J. Marian, B. D. Wirth, R. Schäublin, G. R. Odette, and J. M. Perlado, J. Nucl. Mater. **323**, 181 (2003).

[12] X. Shi, L. Dupuy, B. Devincre, D. Terentyev, and L. Vincent, J. Nucl. Mater. **460**, 37 (2015).

[13] A. Brailsford and R. Bullough, J. Nucl. Mater. **44**, 121 (1972).

[14] A. D. Brailsford and R. Bullough, Philos. Trans. R. Soc. London, Ser. A **302**, 87 (1981).

[15] P. Heald and M. Speight, Acta Metall. **23**, 1389 (1975).

[16] H. Wiedersich, Radiat. Eff. **12**, 111 (1972).

[17] F. Nichols, J. Nucl. Mater. **75**, 32 (1978).

[18] H. Trinkaus, V. Naundorf, B. Singh, and C. Woo, J. Nucl. Mater. **210**, 244 (1994).

[19] W. Phythian, R. Stoller, A. Foreman, A. Calder, and D. Bacon, J. Nucl. Mater. **223**, 245 (1995).

[20] L. Malerba, J. Nucl. Mater. **351**, 28 (2006).

[21] A. E. Sand, S. L. Dudarev, and K. Nordlund, Europhys. Lett. **103**, 46003 (2013).

[22] X. Yi, A. E. Sand, D. R. Mason, M. A. Kirk, S. G. Roberts, K. Nordlund, and S. L. Dudarev, Europhys. Lett. **110**, 36001 (2015).

[23] E. Zarkadoula, G. Samolyuk, H. Xue, H. Bei, and W. J. Weber, Scr. Mater. **124**, 6 (2016).

[24] C. H. Woo and B. N. Singh, Philos. Mag. A **65**, 889 (1992).

[25] A. Y. Dunn, L. Capolungo, E. Martinez, and M. Cherkaoui, J. Nucl. Mater. **443**, 128 (2013).

[26] A. A. Kohnert and B. D. Wirth, J. Appl. Phys. **117**, 154305 (2015).

[27] P. H. Dederichs and K. Schroeder, Phys. Rev. B **17**, 2524 (1978).

[28] C. Woo, J. Nucl. Mater. **159**, 237 (1988).

[29] A. A. Kohnert and L. Capolungo, J. Mech. Phys. Solids **122**, 98 (2019).

[30] C. Varvenne and E. Clouet, Phys. Rev. B **96**, 224103 (2017).

[31] E. Clouet, C. Varvenne, and T. Jourdan, Comput. Mater. Sci. **147**, 49 (2018).

[32] Z. Chang, P. Olsson, D. Terentyev, and N. Sandberg, J. Nucl. Mater. **441**, 357 (2013).

[33] Z. Chang, D. Terentyev, N. Sandberg, K. Samuelsson, and P. Olsson, J. Nucl. Mater. **461**, 221 (2015).

[34] A. A. Kohnert, M. A. Cusentino, and B. D. Wirth, J. Nucl. Mater. **499**, 480 (2018).

[35] S. Dudarev and A. Sutton, Acta Mater. **125**, 425 (2017).

[36] C. N. Tomé, H. A. Cecatto, and E. J. Savino, Phys. Rev. B **25**, 7428 (1982).

[37] I. Margvelashvili and Z. Saralidze, Sov. Phys.-Solid State. **15**, 1774 (1974).

[38] W. G. Wolfer and M. Ashkin, J. Appl. Phys. **47**, 791 (1976).

[39] H. Rauh and D. Simon, Phys. Status Solidi A **46**, 499 (1978).

[40] K. Miller, J. Nucl. Mater. **84**, 167 (1979).

[41] S. L. Dudarev and P.-W. Ma, Phys. Rev. Mater. **2**, 033602 (2018).

[42] D. Carpentier, T. Jourdan, Y. L. Bouar, and M.-C. Marinica, Acta Mater. **136**, 323 (2017).

[43] R. A. Lebensohn, Acta Mater. **49**, 2723 (2001).

[44] A. Vattre, B. Devincre, F. Feyel, R. Gatti, S. Groh, O. Jamond, and A. Roos, J. Mech. Phys. Solids **63**, 491 (2014).

[45] N. Bertin, M. V. Upadhyay, C. Pradalier, and L. Capolungo, Modell. Simul. Mater. Sci. Eng. **23**, 065009 (2015).

[46] N. Bertin and L. Capolungo, J. Comput. Phys. **355**, 366 (2018).

[47] E. Little and D. Stow, J. Nucl. Mater. **87**, 25 (1979).

[48] F. Garner, M. Toloczko, and B. Sencer, J. Nucl. Mater. **276**, 123 (2000).

[49] J. P. Hirth and J. Lothe, *Theory of Dislocations*, 2nd ed. (Wiley, New York, 1982).

[50] E. Clouet, Phys. Rev. B **84**, 092106 (2011).

[51] B. Bako, E. Clouet, L. M. Dupuy, and M. Bletry, Philos. Mag. **91**, 3173 (2011).

[52] V. Jansson, L. Malerba, A. D. Backer, C. Becquart, and C. Domain, J. Nucl. Mater. **442**, 218 (2013).

[53] E. Hayward, C. Deo, B. P. Uberuaga, and C. N. Tomé, Philos. Mag. **92**, 2759 (2012).

[54] P. T. Heald, Philos. Mag. **31**, 551 (1975).

[55] W. G. Wolfer, J. Comput.-Aided Mater. Des. **14**, 403 (2007).

[56] S. Porollo, A. Dvoriashin, A. Vorobyev, and Y. Konobeev, J. Nucl. Mater. **256**, 247 (1998).

[57] L. Mansur, J. Nucl. Mater. **216**, 97 (1994).

[58] R. S. Averback, R. Benedek, and K. L. Merkle, Phys. Rev. B **18**, 4156 (1978).

[59] R. E. Stoller, J. Nucl. Mater. **233–237**, 999 (1996).

[60] H. Xu, Y. N. Osetsky, and R. E. Stoller, J. Nucl. Mater. **423**, 102 (2012).

[61] P.-W. Ma and S. L. Dudarev, Phys. Rev. Mater. **3**, 013605 (2019).

[62] D. Gelles, J. Nucl. Mater. **225**, 163 (1995).

[63] D. Gelles, J. Nucl. Mater. **233–237**, 293 (1996).

[64] R. L. Klueh, Philos. Mag. **98**, 2618 (2018).

[65] R. Schaublin, P. Spatig, and M. Victoria, J. Nucl. Mater. **258–263**, 1178 (1998).

[66] F. HajyAkbary, J. Sietsma, A. J. Böttger, and M. J. Santofimia, Mater. Sci. Eng. A **639**, 208 (2015).

[67] V. Dubinko, A. Abyzov, and A. Turkin, J. Nucl. Mater. **336**, 11 (2005).

[68] T. Jourdan, J. Nucl. Mater. **467**, 286 (2015).

[69] K. Schroeder and K. Dettmann, Z. Phys. B **22**, 343 (1975).

[70] B. C. Skinner and C. H. Woo, Phys. Rev. B **30**, 3084 (1984).